Available online at www.sciencedirect.com
SCIENCE DIRECT®
Journal of Nuclear Materials 348 (2006) 191–204
journal of nuclear materials
www.elsevier.com/locate/jnucmat

Comprehensive investigation of the corrosion state of the heat exchanger tubes of steam generators. Part II. Chemical composition and structure of tube surfaces

Z. Homonnay [a,*], E. Kuzmann [b], K. Varga [c,*], Z. Németh [c], A. Szabó [c], K. Radó [c], K.É. Makó [d], L. Kövér [e], I. Cserny [e], D. Varga [e], J. Tóth [e], J. Schunk [f], P. Tilky [f], G. Patek [f]

[a] *Department of Nuclear Chemistry, Faculty of Science, Eötvös University, H-1518 Budapest, P.O. Box 32, Hungary*
[b] *Research Group for Nuclear Methods in Structural Chemistry, Hungarian Academy of Sciences, Eötvös University, Budapest, Hungary*
[c] *Department of Radiochemistry, University of Veszprém, H-8201 Veszprém, PO Box: 158, Hungary*
[d] *Department of Silicate and Materials Engineering, University of Veszprém, Veszprém, Hungary*
[e] *Section of Electron Spectroscopy, Institute of Nuclear Research, H-4001 Debrecen, Hungary*
[f] *Paks NPP, Paks, Hungary*

Received 8 October 2003; accepted 16 September 2005

Abstract

In the frame of a project dealing with the comprehensive study of the corrosion state of the steam generators of the Paks Nuclear Power Plant, Hungary, surface properties (chemical and phase compositions) of the heat exchanger tubes supplied by the power plant were studied by Mössbauer spectroscopy (CEMS), X-ray diffraction (XRD) and X-ray photoelectron spectroscopy (XPS) methods. The work presented in this series provides evidence that chemical decontamination of the steam generators by the AP-CITROX technology does exert a detrimental effect on the chemical composition and structure of the protective oxide film grown-on the inner surfaces of heat exchanger piping. As an undesired consequence of the decontamination technology, *a 'hybrid' structure of the amorphous and crystalline phases is formed in the outermost surface region (within a range of 11 μm)*. The constituents of this 'hybrid' structure exhibit great mobility into the primary coolant under normal operation of the VVER type reactor.

PACS: 82.55.+e; 81.65.Kn

1. Introduction

The corrosion of austenitic stainless steel piping of steam generators (SGs) subjected to the effect of primary coolant in a nuclear reactor is basically determined by the protective surface oxide layer as

* Corresponding authors. Tel.: +36 1 372 2914; fax: +36 1 372 2592 (Z. Homonnay), fax: +36 88 427681 (K. Varga).
E-mail addresses: homonnay@ludens.elte.hu (Z. Homonnay), vargakl@almos.vein.hu (K. Varga).

0022-3115/$ - see front matter © 2005 Elsevier B.V. All rights reserved.
doi:10.1016/j.jnucmat.2005.09.013

well as by the structure of the bulk steel. Under various circumstances, the paramagnetic austenitic γ-phase may transform into ferromagnetic α-phase (ferrite, martensite) [1–4]. The ferrite (martensite) content has a strong influence on the sensitivity of steel towards stress-corrosion cracking (SCC) and intergranular stress-corrosion cracking (IGSCC) ([1–3,5–7] and references therein). Therefore, if the γ to α phase transformation is significant and is spread over a large number of heat exchanger tubes, the emerged metallographic and corrosion consequences will negatively affect the conditions of safe operation of the SGs, and thereby the chance for an extended operational life time of the whole reactor system [1,5–8]. The performance of the steam generator piping in water-cooled nuclear reactors was extensively reviewed in the last three decades ([7–10] and references therein). It has been demonstrated that the leading cause of tube failure is SCC at the primary circuit side, and SCC and/or IGSCC at the secondary circuit side.

As part of a comprehensive investigation of the SGs at Paks Nuclear Power Plant (Paks NPP), 22 specimens of austenitic stainless steel piping were studied in order to characterize their metallographic and corrosion state. The methods applied were as follows: electrochemistry (voltammetry), SEM-EDX, CEMS (conversion electron Mössbauer spectroscopy), XRD, and XPS. The general corrosion state of these samples with special attention to their earlier chemical treatment(s) by the AP-CITROX decontamination procedure has been discussed in Part I of this series [11]. In the present work, we report some new findings on the chemical and phase composition of the surface layers obtained by CEMS, XRD, and XPS studies of the heat exchanger tubes.

2. Experimental section

2.1. CEMS analysis of the surface oxide layers

Twenty two samples cut out from the heat exchanger tubes of the steam generators were measured by conversion electron Mössbauer spectroscopy (CEMS) in order to identify the iron containing phases of the surface oxide layers. The main characteristics and notations of the samples are listed in Table 1 of our previous report [11]. The application of CEMS in this case is based on the recoilless nuclear absorption of the 14.4 keV γ-rays of ^{57}Fe in the surface oxide layer, followed by the emission of conversion electrons upon de-excitation of the ^{57}Fe nucleus. The surface selectivity of the measurement is guaranteed by the detection of low energy conversion electrons (<7 keV).

Table 1
Percentage phase distribution on the specimens' surfaces determined from the CEMS spectra

Sample	Phases (m/m%*)			
	Steel (austenite)	γ-FeOOH/ $Fe(OH)_3$	Fe_3O_4	α-Fe_2O_3
1	50	32	18	–
2	75	11	14	–
3	29	71	–	–
4	38	62	–	–
5	17	56	27	–
6	20	36	44	–
7	14	40	46	–
8	40	44	16	–
9	42	42	16	–
10	25	36	24	15
11	13	63	24	–
12	57	23	–	20
13	54	46	–	–
14	53	13	13	21
15	14	13	73	–
16	12	12	76	–
17	26	20	54	–
18	50	27	–	23
19	20	18	15	47
20	21	17	27	35
21	22	19	22	37
22	93	7	–	–

* Percentage Fe-content of the sample assigned to the indicated phase.

To prepare samples for the Mössbauer measurements, 2 cm long pieces were cut out from the tubes and then halved in axial direction. The halves were then carefully pressed mechanically to get a flat surface (in order to ensure an optimal distance between the sample surface and the anode wire of the proportional detector used) while keeping the inner surface (primary circuit side) free from any damage. In case of accidental damage, the damaged surface was covered with an organic paint so that this part of the sample did not give any Mössbauer signal. Most CEMS measurements were carried out on the inner surface of the tubes. (For measurements on the outer surface, mechanical shaping was not necessary.)

The CEMS spectra were recorded at room temperature with a conventional Mössbauer spectrometer (Wissel) in constant acceleration mode. The conversion electrons were detected with a constant-flow type proportional counter specially

designed for CEMS technique (Ranger). The counter gas was a mixture of 96% He and 4% methane. A ^{57}Co(Rh) source provided the γ-rays. Calibration was done by measuring an α-Fe foil in transmission mode, which is the reference of the isomer shifts given in this paper.

Due to the absorption of the conversion electrons in the sample, information can be obtained from a maximum of ~300 nm thick surface layer. The average error of the determination of the phase composition is ±5%; however, this figure does not include the depth dependent sensitivity of the detection process. Therefore, the phase composition (i.e., the distribution of the iron content of the sample among different phases) obtained is always an integral composition of the 300 nm thick surface layer, which contains a roughly (negative) exponential weighing according to the depth of the particular phase.

One has to mention here that the mechanical shaping of the tube specimens may cause cracking of the oxide layer, and therefore, the bulk steel may open up for the counter, resulting in overestimation of the austenitic steel in the (~300 nm) surface layer. Taking into account the outer and inner diameter of the tubes, 20% of the bulk steel may open up at maximum for the detection process when the tube is completely flattened if the cracks reach the bulk material everywhere on the surface. In our measurements, cracking of the shaped surface was never observed, nor any peeling of the oxide layer. The contribution of the subspectrum of the austenitic steel phase in the CEMS spectra, however, varied from 5% to 90%. This shows that the mechanical shaping must have a minor effect on the CEMS phase analysis.

2.2. XRD phase analysis

X-ray diffractometry (XRD) as a standard technique in metallurgy was applied to show the formation of the α-phase in the austenitic steel. The 2 cm long pieces of the heat exchanger tubes were cut into halves but were not further shaped as for the CEMS measurements. The XRD measurements were carried out with a PHILIPS PW3710 type diffractometer (CuKα or CoKα radiation, voltage: 40 kV, current: 40 mA, goniometer speed: 0.02°/s).

Both the inner and outer surfaces were analyzed for almost all samples.

Taking into account the absorption characteristics of the CuKα (CoKα) radiation (~8 keV), the phase analysis refers to a ~30 μm thick surface layer, which is approximately 100 times larger than in the case of the CEMS method. The exact quantitative phase analysis is hindered by depth dependent sensitivity of the method and, in addition, by texture of the samples, possible existence of amorphous components, uneven surface, etc. The relative error of the determination of crystalline phases may be estimated as ±5%.

Non-crystalline phases, like amorphous Fe-oxides, -oxihidroxides may not be analyzed. Their presence is indicated mostly by line broadening and increase in the baseline intensity.

2.3. XPS analysis of the structure and chemical composition of surface oxide layers

Structure and chemical composition of the outermost films grown-on the inner surfaces of heat exchanger tubes decontaminated in 2001 – about one year before sampling (see Table 1 in [11]) – were studied by X-ray photoelectron spectroscopy (XPS). The XPS measurements were carried out by ESA-31 (ATOMKI, Hungary) type spectrometer [12] on 'as-received' samples as well as on surfaces obtained by ion sputtering. For these studies, rectangular (10 mm × 10 mm) pieces of austenitic stainless steel were cut out from the tube specimens without mechanical deformation. Al-K_α radiation with energy of 1486.6 eV was used as primary X-ray source. The sputtering was performed with 2 keV argon ions (ion current was 140 μA/cm^2) at a rate of about 1.4 nm/min. The total thickness of the oxide film removed from the surface of each sample by Ar ion sputtering was approximately 105 nm. The photoelectrons analyzed were emitted in a narrow solid angle around the normal vector of the sample surface. The XPS spectra measured were evaluated by making use of 'EWA: a spectrum evaluation program for XPS/UPS' [13].

3. Results

3.1. Phase analysis of the surface oxide layers by CEMS

Figs. 1 and 2 show ^{57}Fe-CEMS spectra of some selected samples. The results of the phase analysis are summarized in Table 1 for all the 22 samples. Some trends may be observed as follows.

It was found that on the inner surface of samples 15–17 and 19–21 the dominant phases (i.e., those with a total contribution of over 50%) are magnetite

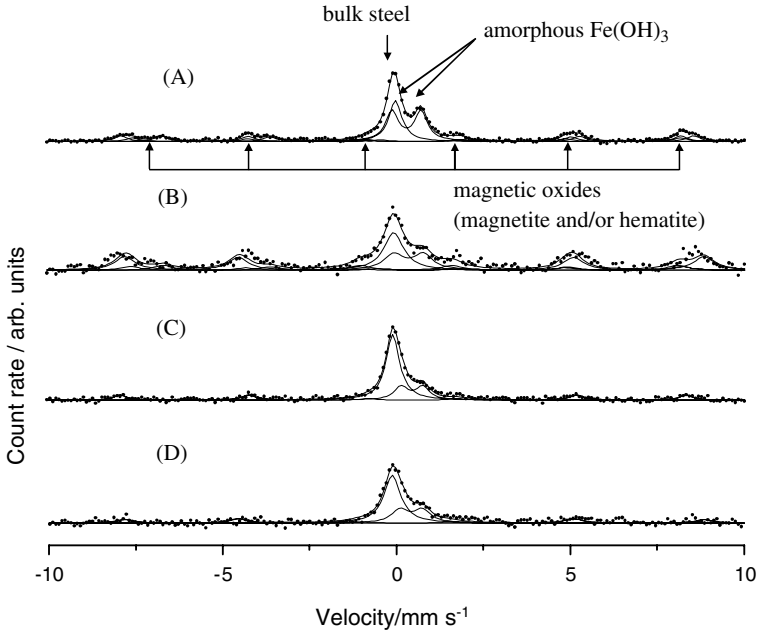

Fig. 1. CEMS spectra measured on the inner surface of samples 10 (A), 21 (B), 12 (C) and 18 (D).

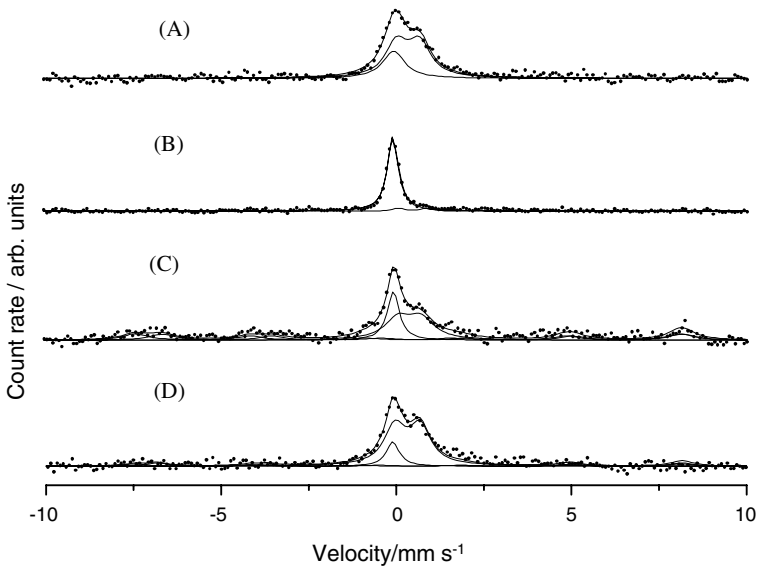

Fig. 2. CEMS spectra measured on the inner surface of samples 3 (A), 22 (B), 6 (C) and 11 (D).

and/or hematite (see Fig. 1(B) for sample 21). The magnetic phases are dominant, although remain below 50% in sample 10 (Fig. 1(A)). Magnetite is represented by two sextets in the Mössbauer spectra due to two different cationic sites for iron in the inverse spinel structure, while hematite can be described with one sextet only. The Mössbauer parameters obtained for these phases (especially for magnetite) were slightly different from the literature data on the pure compounds, which can be attributed to the effect of Cr- and Ni-substitution. It is also noteworthy that the approximate intensity ratio of the two sextets of magnetite is normally I_H:$I_L = 1$:2, where I_H is the intensity of the sextet with higher magnetic field (representing Fe^{3+} at the tetrahedral site, A, of the unit cell of magnetite)

and I_L is the intensity of the sextet with lower magnetic field (representing Fe^{3+} *and* Fe^{2+} at the octahedral site, B, of the unit cell of magnetite), but we have found in our samples roughly the opposite ratio. Since it is well known that Cr^{3+} and Ni^{2+} is ready to substitute for iron at site B of the spinel structure, it is logical to assume such substitution in our case, on the surface of a Cr–Ni–steel.

Magnetite was absent on the inner surface of samples 12 and 18 (Fig. 1(C) and (D), respectively), while on samples No. 3, 4, 13, and 22 magnetic phases could not be found at all within experimental uncertainty (see Fig. 2(A) and (B)).

The phase analysis of the samples which were subjected to a decontamination process one or two year before this CEMS study (samples No. 1–2, 5–9, and 11), revealed various amounts of magnetite besides the austenitic bulk steel in the upper 300 nm layer. In these samples the dominant magnetic phase is undoubtedly the magnetite (due to statistics of the spectra, the presence of 5–10% hematite cannot be excluded, see Fig. 2(C) and (D)).

In addition to the magnetic phases and/or the bulk steel, the presence of another paramagnetic phase was made obvious by the spectrum evaluations in all samples. The doublet assigned to this phase could be evaluated by an isomer shift of $\delta = 0.35$–0.45 mm/s and a quadrupole splitting of $\Delta = 0.6$–0.8 mm/s. These parameters practically correspond to lepidocrocite (γ-FeOOH) or amorphous iron(III)-hydroxide ($Fe(OH)_3$). Since XRD did not indicate reflections of crystalline lepidocrocite, we assigned the doublet to amorphous $Fe(OH)_3$.

The presence of the α-phase (ferrite, martensite) could not be confirmed in the upper 300 nm layer besides the oxide phases by CEMS. Interestingly, however, when the surface was cleaned from the oxide layer (inner and outer surface of sample 4, outer surface of sample 20), the ferrite phase showed up. The relative amount of this phase (i.e., that of iron contained in the phase) was very significant, namely 60% and 50% on the outer and inner surface of sample 4, respectively, and 22% on the outer surface of sample 20.

3.2. XRD phase analysis

The inner and outer surfaces of all the samples (except samples 4, 5, 13, 14, and 20) were investigated by XRD. Some selected diffractograms are shown in Figs. 3–5. The following notations are used in the diffractograms:

SS – steel 304 ($Cr_{0.19}Fe_{0.7}Ni_{0.11}$) /PDF 33-0397/
M – magnetite (Fe_3O_4) /PDF 19-0629/
H – hematite (Fe_2O_3) /PDF 33-0664/
Fe – ferrite (Fe) /PDF 6-0696/
Ma – martensite ($C_{0.09}Fe_{1.91}$) /PDF 44-1292/
L – lepidocrocite (γ-FeOOH) /PDF 8-98/
K – calcite ($CaCO_3$) /PDF 5-586/
A – amesite ($(Mg,Fe)_2Al(Si,Al)_2O_5(OH)_4$) /PDF 37-0429/

The abundance of the phases in percentage is compiled in Table 2.

The primary goal of the XRD studies was to detect the α-phase (if any) at the inner and outer

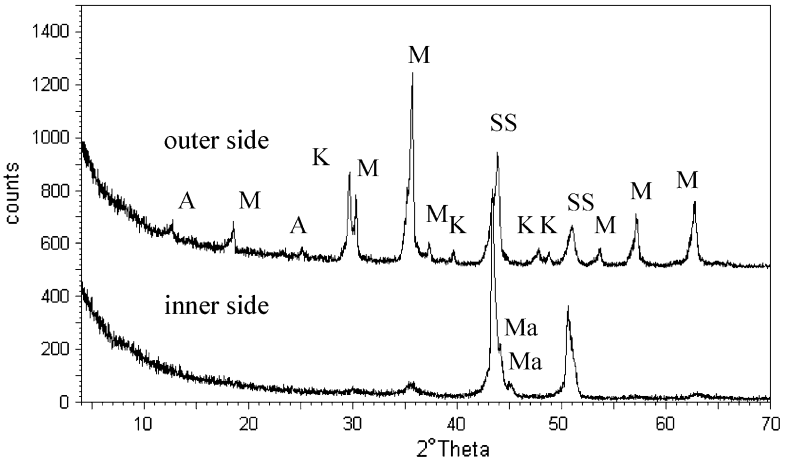

Fig. 3. XRD pattern measured on the outer and inner surface of sample 1, using CuK_α radiation. (See Table 2 for notations.)

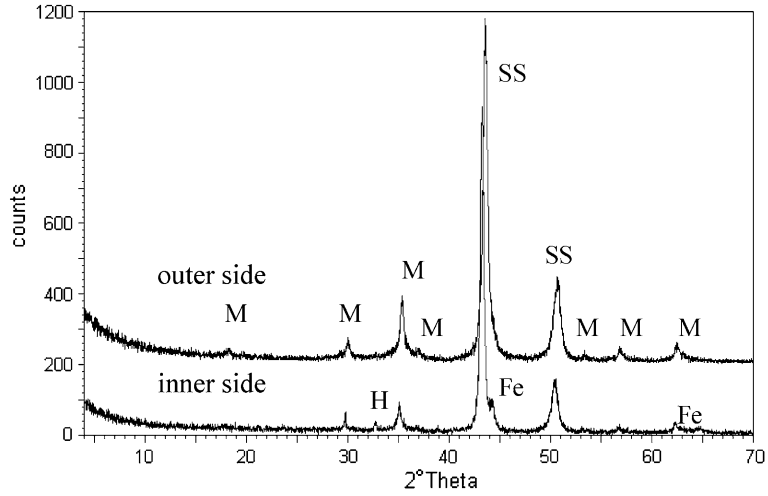

Fig. 4. XRD pattern measured on the outer and inner surface of sample 18, using CuK_α radiation. (See Table 2 for notations.)

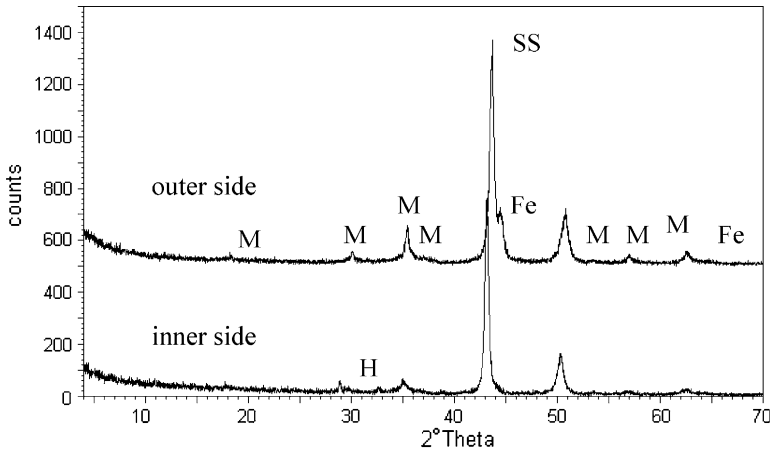

Fig. 5. XRD pattern measured on the outer and inner surface of sample 19, using CuK_α radiation. (See Table 2 for notations.)

surfaces of the samples. In the group of the investigated samples, the ferrite (martensite) phase could be undoubtedly shown on the inner surface of samples 1, 6, 7, 8, and 18 (see e.g. Figs. 3 and 4), as well as on the outer surface of samples 16, 17, and 19 (Fig. 5). It is to be noted that the presence of the α-phase was convincingly shown on both the inner and outer surface of the reference steel specimen (sample 22). Owing to the partial overlapping of the main XRD reflections of the austenite and ferrite phases, the presence of ferrite in the other samples cannot be excluded in a percentage up to ~7%.

Since the penetration depth of the applied X-rays is about two orders of magnitude higher than that of the conversion electrons, one may conclude that the γ to α phase transformation is a bulk phenomenon in the samples studied.

3.3. XPS studies of oxide layers

Samples having been subjected to decontamination the AP-CITROX method about a year before sampling (No. 7, 9, and 11 in Table 1 in [11]) were studied by XPS. The composition of the oxide layer as a function of depth measured on tube samples 9 and 11 is given in Figs. 6 and 7, respectively. It should be emphasized that the XPS results obtained for different samples decontaminated in 2001 are basically similar, irrespective of the location they

Table 2
Percentage distribution of the crystalline phases on the specimens' surfaces determined from XRD data

Sample	SS Steel 304	M Magnetite	H Hematite	Fe Ferrite	K Calcite	A Amesite	Ma Martensite	L Lepidocrocite
1 outer side	37	56	–	–	5	2		–
1 inner side	77	4	–	–	–	–	19	–
2 outer side	40	59	–	–	–	–	–	–
2 inner side	97	3	–	–	<1	–	–	–
3 outer side	90	10	–	–	–	–	–	–
3 inner side	40	60	–	–	–	–	–	–
6 outer side	9	84	–	–	7	–	–	–
6 inner side	82	7	–	11	–	–	–	–
7 outer side	78	22	–	–	–	–	–	–
7 inner side	76	18	–	6	–	–	–	–
8 outer side	40	59	–	–	<1	–	–	–
8 inner side	84	4	–	12	–	–	–	–
9 outer side	64	36	–	–	–	–	–	–
9 inner side	94	6	–	–	–	–	–	–
10 outer side	95	4	–	–	–	–	–	1
10 inner side	87	12	1	–	–	–	–	–
11 outer side	76	23	–	–	1	–	–	–
11 inner side	84	16	–	–	–	–	–	–
12 outer side	80	20	–	–	–	–	–	–
12 inner side	95	5	–	–	–	–	–	–
15 outer side	79	23	–	–	<1	–	–	–
15 inner side	96	4	–	–	–	–	–	–
16 outer side	78	13	–	7	<1	–	–	–
16 inner side	82	14	3	–	<1	–	–	–
17 outer side	52	41	–	4	3	–	–	–
17 inner side	82	17	–	–	–	–	–	–
18 outer side	85	15	–	–	–	–	–	–
18 inner side	85	6	2	7	–	–	–	–
19 outer side	67	10	–	23	–	–	–	–
19 inner side	93	6	1	–	–	–	–	–
21 outer side	90	10	–	–	–	–	–	–
21 inner side	76	22	2	–	–	–	–	–
22 outer side	90	3	–	7	–	–	–	–
22 inner side	87	–	–	13	–	–	–	–

were cut out from the steam generator. It is obvious from these figures that the dominant components of the outermost 105 nm thick oxide layers are O, Cr, Ni, Fe and C. The depth distribution of these components exhibits saturation characteristic in the deeper oxide region (below approximately 30 nm). A careful analysis of the XPS depth profiles in Figs. 6 and 7 reveals that Cr (mainly in the forms of Cr_2O_3, $Cr(OH)_3$ and CrO(OH)) is dramatically enriched in the oxide layers. Specifically, the Cr to Fe ratio approaches 2 in the entire range of surface oxides studied (see Fig. 8). Examinations by XPS on these steel samples indicate the existence of various types of iron-oxides (FeOOH, Fe_2O_3, and Fe_3O_4). While in the outermost range of the oxide films, the relative fraction of FeOOH and $Cr(OH)_3$ and/or CrO(OH) are large, in the deeper region Fe_3O_4 and Cr_2O_3 are the predominant contributors to the XPS peaks. Metallic Cr and Fe (appearing partly as a consequence of reduction during ion sputtering) can be detected only in the spectra obtained from the deeper parts of the oxide layer. An enrichment in Ni (mainly in metallic Ni and $Ni(OH)_2$) can also be observed in the total surface region studied.

It is of special importance that the concentration of carbon is found higher than 10% (atomic concentration) in the entire oxide film. The most intense carbon signal can be detected from just below the surface (in the outermost 40 nm thick oxide layer). It is obvious that such a large amount of carbon cannot be interpreted as some surface pollutant from air (e.g., CO_2). Moreover, analysis of the C 1s and O 1s XPS peaks provides strong indication that the carbon contamination in the surface oxides is probably caused by the remnants of oxalic and/or

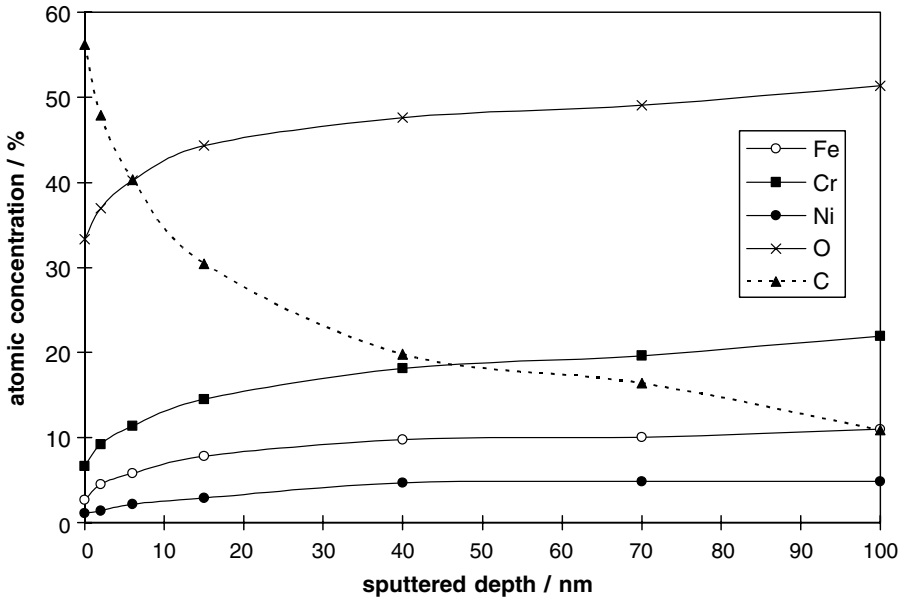

Fig. 6. XPS depth profiles measured on the inner surface of sample 9.

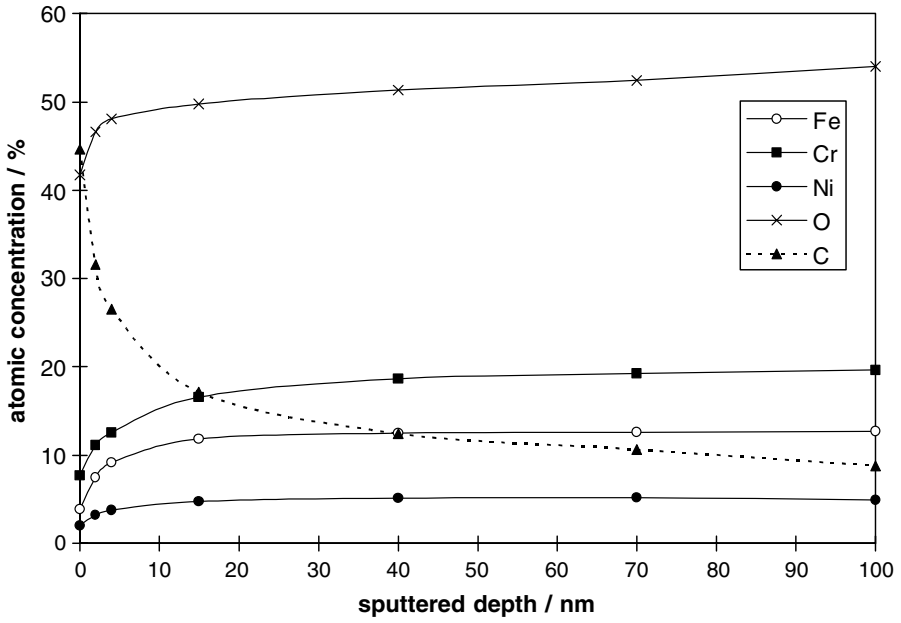

Fig. 7. XPS depth profiles measured on the inner surface of sample 11.

citric acids which is used in step 4 of the AP-CITROX decontamination procedure [11].

All these results, in accordance with the CEMS and XRD data, suggest that *some amorphous phases containing (or mixed with) carbon compounds are most likely segregated among the crystalline constituents of the surface films*, as an undesired consequence of the chemical decontamination of the heat exchanger piping of the SGs.

4. Discussion

Explanation of the structure and composition of the oxide layers formed on the inner surfaces of the

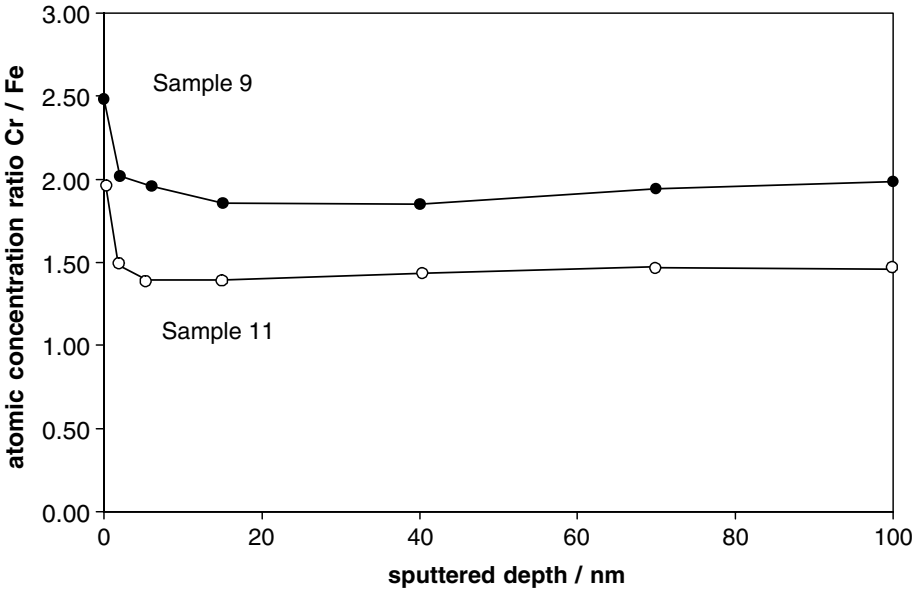

Fig. 8. Cr/Fe ratio on the inner surface of samples 9 and 11.

heat exchanger tubes is possible by comparing the CEMS, XRD and XPS data. As demonstrated in Tables 1 and 2, the results of the CEMS and XRD phase analysis proved to be different. The difference in the quantities of the various phases can be attributed to the strong depth dependence of the abundance of these phases, taking into account that the characteristic thickness from which the information on the phase composition can be obtained is ~0.3 μm for CEMS, and ~30 μm for XRD. The estimated statistical errors in the relative compositions are ±5% for both methods, however several additional factors hinder the direct comparison (Mössbauer–Lamb factors, different depth selectivity profiles, texture, etc.).

In general, it can be stated that XRD underestimates, while CEMS overestimates the abundance of the oxide phases relative to the bulk steel (at least, as compared to each other). This is compensated to some extent by the fact that the XRD signal represents the lattice of a phase, while the CEMS signal represents only the Fe content in it. For example, the CEMS signal of magnetite decreases upon chromium substitution for iron, while the XRD signal of the phase is practically not affected. This results in varying sensitivity.

Crystallite size effects also contribute to the different sensitivity of the two methods. XRD cannot detect phases under a certain crystallite size which is still observable for CEMS (a local probe method). Thus, amorphous $Fe(OH)_3$ cannot be observed by XRD while it can well be detected by CEMS.

Sometimes CEMS is not reliable in detecting phases because of overlapped Mössbauer lines. For instance, in the presence of the large amounts of magnetite and/or hematite the ferrite phase may remain hidden up to about 10%. This situation is even more serious, if the ferrite is enriched in Cr and/or Ni. On the other hand, the texture of specimen's surface (preferential orientation of the crystallites in the sample) can strongly influence the determination of relative abundances of the various phases in XRD.

Taking into account all these possible effects, the results of XRD and CEMS phase analysis compiled in Tables 1 and 2 do not contradict each other, and they may be interpreted in a reasonable way.

The main characteristics of the phase analysis of the samples originating from 22 different SGs, together with the most important experimental data presented in the first part of this series [11], are summarized in Table 3. As has been emphasized earlier, the number of samples studied is rather low, and the selection of sampling locations in SGs was not done in a way that it might be considered as a representative study (this could be almost impossible in case of a reactor still in operation). Despite the limited number of tube samples, some general statements (in addition to those presented in our previous

Table 3
Main corrosion and metallographic characteristics of the steel specimens studied

Sample	Average corrosion rate of the inner surface (mm/year)	Thickness of the oxide layer formed on the inner surface (μm)	'CEMS' phase distribution of the oxide layer formed on the inner surface (%)	Presence of the α-phase (ferrite, martensite)[a]		Year of decontamination	Year of sampling	Year of investigation
				On the inner surface	On the outer surface			
1	≈0.0005	⩽0.5	$Fe(OH)_3$ – 32 Fe_3O_4 – 18 Austenite – 50	+ (XRD, 19%)	– (XRD)	2001	2002	2002
2	≈0.0004	0.2–0.9	$Fe(OH)_3$ – 11 Fe_3O_4 – 14 Austenite – 75	– (XRD)	– (XRD)	2001	2002	2003
3	≈0.0035	8–11	$Fe(OH_3)_3$ – 71 Austenite – 29	– (XRD)	– (XRD)	1996, 1997	2001	2001
4	≈0.0039	NA	$Fe(OH)_3$ – 62 Austenite – 38	+ (CEMS, 50%)	+ (CEMS, 61%) (XRD)	1996	2000	2000
5	≈0.0006	3–5	$Fe(OH)_3$ – 56 Fe_3O_4 – 27 Austenite – 17	NA	NA	1996	1997	2003
6	≈0.0004	1.3–4	$Fe(OH)_3$ – 36 Fe_3O_4 – 44 Austenite – 20	+ (XRD, 11%)	– (XRD)	2001	2002	2002
7	≈0.0004	1–4.5	$Fe(OH)_3$ – 40 Fe_3O_4 – 47 Austenite – 13	+ (XRD, 6%)	– (XRD)	2001	2002	2002
8	≈0.0004	7–11	$Fe(OH)_3$ – 44 Fe_3O_4 – 16 Austenite – 40	+ (XRD, 12%)	– (XRD)	2001	2003	2003
9	≈0.0004	3–5 (Fe-oxide deposits)	$Fe(OH)_3$ – 42 Fe_3O_4 – 16 Austenite – 42	– (XRD)	– (XRD)	2001	2002	2002
10	≈0.0005	<0.5	$Fe(OH)_3$ – 36 Fe_3O_4 – 24 Fe_2O_3 – 15 Austenite – 25	– (XRD)	– (XRD)	–	1999	2001

11	≈0.0006	NA	$Fe(OH)_3$ – 63 Fe_3O_4 – 24 Austenite – 13	– (XRD)	– (XRD)	2001	2002	2002
12	≈0.0006	0.2–5	$Fe(OH)_3$ – 23 Fe_2O_3 – 20 Austenite – 57	– (XRD)	– (XRD)	2001	2001	2001
13	≈0.0018	NA	$Fe(OH)_3$ – 46 Austenite – 54	NA	NA	1993	2000	2000
14	≈0.0003	<0.5	$Fe(OH)_3$ – 13 Fe_3O_4 – 13 Fe_2O_3 – 21 Austenite – 53	NA	NA	–	2000	2000
15	≈0.0002	<0.5	$Fe(OH)_3$ – 13 Fe_3O_4 – 73 Austenite – 14	– (XRD)	– (XRD)	–	2003	2003
16	≈0.0001	<0.5	$Fe(OH)_3$ – 12 Fe_3O_4 – 76 Austenite – 12	– (XRD)	+ (XRD, 7%)	–	1999	2003
17	≈0.0001	<0.5	$Fe(OH)_3$ – 20 Fe_3O_4 – 54 Austenite – 26	– (XRD)	+ (XRD, 4%)	–	2003	2003
18	≈0.0008	<0.5	$Fe(OH)_3$ – 27 Fe_2O_3 – 23 Austenite – 50	+ (XRD, 7%)	– (XRD)	–	2001	2001
19	≈0.0004	⩽0.5	$Fe(OH)_3$ – 18 Fe_3O_4 – 15 Fe_2O_3 – 47 Austenite – 20	– (XRD)	+ (XRD, 23%)	–	1998	2001
20	<0.0018	<0.5	$Fe(OH)_3$- 18 Fe_3O_4 – 26 Fe_2O_3 – 35 Austenite – 21	NA	+ (CEMS, 22%)	–	2000	2000
21	≈0.0007	<0.5	$Fe(OH)_3$ – 19 Fe_3O_4 – 22 Fe_2O_3 – 37 Austenite – 22	– (XRD)	– (XRD)	–	2001	2001
22	≈0.0004	<0.5	$Fe(OH)_3$ – 7 Austenite – 93	+ (XRD, 13%)	+ (XRD, 7%)	Inactive ref. sample	1982	2001

[a] NA: not available; –: not detectable; +: detectable.

paper [11] on the overall corrosion state) could be drawn:

(1) Comparing the phase compositions of the inner (primary circuit side) and outer (secondary circuit side) surfaces determined by XRD, one may conclude that despite the reductive water chemistry of the heat carrier medium, magnetite is very rarely found in the oxide layer formed on the inner surfaces. In contrast, magnetite is a dominant phase at the outer surface. This observation can be explained if one takes into account that the steel used in the secondary circuit is basically carbon steel. A common phase component on the inner surface of all investigated samples is the amorphous $Fe(OH)_3$. Its dominance is most characteristic for samples No. 3, 4, and 13 which were decontaminated by the AP-CITROX procedure a few years before the sampling. These samples showed the highest average corrosion rate [11]. At the same time, it is difficult to understand why the other samples, which exhibit better corrosion resistance, contain some amount of amorphous $Fe(OH)_3$ either. A possible explanation is that formation of the amorphous $Fe(OH)_3$ phase is rather connected to transient periods of the reactor operation as well as to the storage conditions (influence of the humid air) of the tube samples, and not solely to the normal operational circumstances in the VVER reactor.

(2) The presence of α-phase (ferrite) in the austenitic structure was indicated in 11 specimens out of the 17 investigated samples. For 10 samples out of the 11, the ferrite phase seemed to be present in the bulk, not only at the surface region. Their abundance in the 0.3 μm thick surface layer was in the range 22–61%; however, in the case of seven samples the amount of the α-phase went over 10% even in the upper 30 μm surface layer. It is of special importance to note that the presence of ferrite phase has been detected on the inner and outer surfaces of the reference sample, too. Correlation between the presence/extent of the $\gamma \rightarrow \alpha$ phase transformation and the general corrosion state of the samples could not be found. The abundance of the α-phase in samples with different corrosion characteristics is practically the same, and the selection of the inner or the outer surface is also irrelevant. It is well documented that the formation of the ferrite (martensite) phase may be induced by cold rolling, shaping, polishing, welding, as well as probably by irradiation and chemical decontamination ([1–3,5–7] and references therein).

(3) Two models for the structure of the protective surface layer grown on the samples never-decontaminated and decontaminated by the AP-CITROX procedure have been elaborated. The schematic models shown in Fig. 9 are based on the comprehensive studies by the CEMS, XPS, XRD and SEM-EDX techniques. The mechanism of the formation of the surface film illustrated in Fig. 9 may be described as follows.

Under normal operating conditions of the primary circuit of VVER-type reactors (high pressure, high temperature, and reductive water chemistry) the thermodynamically less stable alloying elements (mainly Fe) are dissolved into the primary coolant, and partially form a more or less stable oxide layer (mainly magnetite and hematite) at the outermost surface. As a result of the selective dissolution, the surface area (within a range of few microns) of the bulk steel will be Fe-depleted and, consequently, Cr- and Ni-enriched. The Cr- and Ni-enrichments apply not only to the austenitic phase but also to the magnetite, resulting in the formation of mixed spinel-type oxides to be considered as the predominant constituents of the protective surface films.

It is very likely that the protective oxide layer could not be re-created and stabilized after the chemical decontamination of the steam generator. Specifically, a protective layer of uniform thickness with so-called 'duplex' (laminated) structure did not form. As demonstrated by the CEMS phase analysis and the XPS depth profiles, *both austenite and spinel phases of low Fe content and of relatively high Cr- and Ni-content can be found simultaneously in the surface film (even within the outermost surface range of 300 nm)*. Moreover, as has been discussed in our previous paper [14,15], the chemical decontamination can be considered to be responsible for the great extent of the formation of amorphous iron-hydroxides and oxihidroxides ($Fe(OH)_3$ and/or FeOOH) at the interface region. As follows from the depth distributions of carbon shown in Figs. 6 and 7 as well as from the metallographic cross sections presented in [11], the *amorphous phases are presumably segregated among the crystalline constituents of the surface films*.

In summary, the chemical decontamination of the SGs by the AP-CITROX procedure does exert an undesired transformation effect on the stable constituents of surface layer (magnetite, hematite, spinel and even the bulk austenite), leading to the formation of *a 'hybrid' structure of the amorphous and crystalline phases*. The formation of above

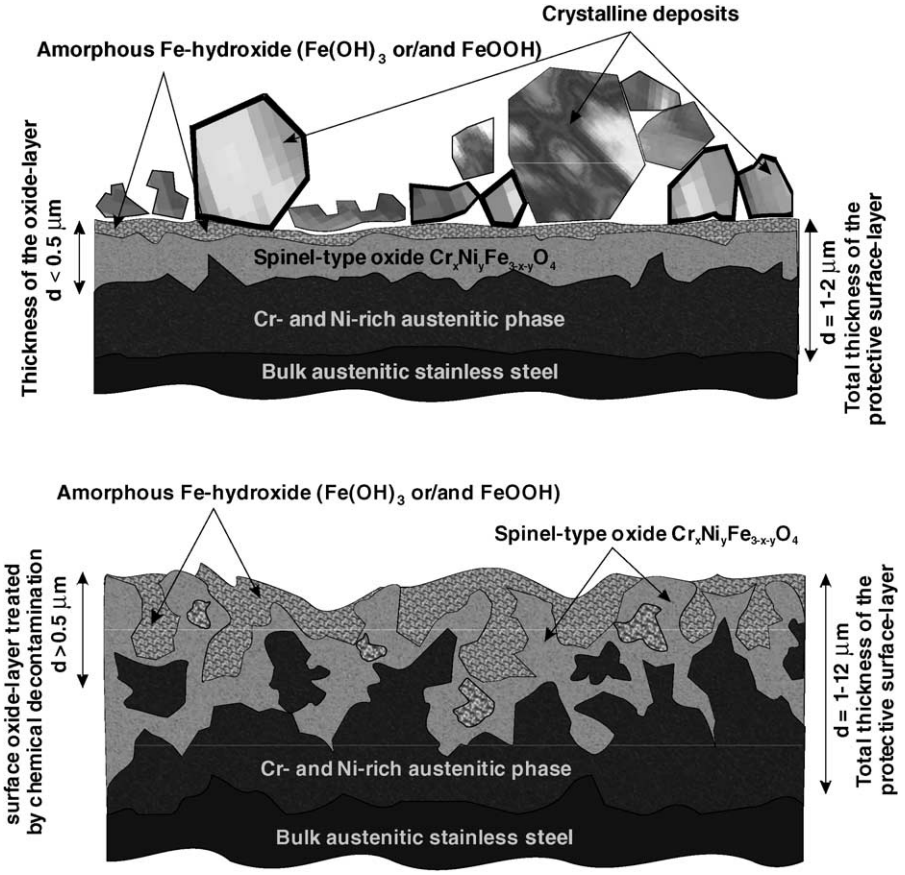

Fig. 9. Hypothetical models of the surface structure of never-decontaminated and decontaminated samples.

mobile oxide-layer has increased significantly the amount of corrosion products in the primary circuit of a nuclear reactor of the Paks NPP, resulting in magnetite deposition on fuel assemblies [14,15].

5. Conclusions

In the frame of a project dealing with the comprehensive study of the corrosion state of the steam generators of the Paks Nuclear Power Plant, Hungary, surface properties (chemical and phase compositions) of the heat exchanger tubes supplied by the power plant were investigated by CEMS, XRD and XPS methods. Based on the experimental findings, two models for the structure of the protective surface layer grown on the samples never-decontaminated and decontaminated by the AP-CITROX procedure were elaborated. Moreover, possible mechanism of the formation of the various oxide structures was proposed.

The work presented in this series provides evidence that chemical decontamination of the steam generators by the AP-CITROX technology does exert a detrimental effect on the chemical composition and structure of the protective oxide film grown-on the inner surfaces of heat exchanger piping. The oxide-layer formed on the inner surfaces of decontaminated samples is thick (up to 11 μm), and has a 'hybrid' structure of the amorphous and crystalline phases (such as amorphous Fe-oxide (-hydroxide), austenite and spinell phases of high Cr- and Ni-contents). Accelerated corrosion rate for the decontaminated steel surfaces occurs in VVER's environment during normal operation (up to four years) to yield a gradually thicker 'hybrid' structure, which influences significantly the amount of the corrosion products in the primary circuit. Therefore, *decontamination process restrictions and modifications to minimize corrosion damages should be defined*, and there is ample data available now for utilities to select a CITROX based process for particular application. In this regards, however, it is of special importance to highlight all the advantages and the risk factors of the Fe-oxide dissolution

with oxalic acid reagents (see e.g. [14,16] and references cited therein).

Acknowledgements

This work was supported by the Paks NPP Co. Ltd. (Paks, Hungary), and the Hungarian Science Foundation (OTKA Grant No. T 047219 and T043687). Technical help in CEMS measurements by S. Stichleutner is acknowledged.

References

[1] V.V. Geraszimov, A.S.Z. Monahov, Materiali Jadernoj Techniki, Atomizdat, Moscow, 1981.
[2] L. Habraken, J.L. de Brouwer, Bases de la metallographie, Academiques Europeennes, Bruxelles, 1968.
[3] R.C. Newman, Stress-corrosion cracking mechanism, in: P. Marcus, J. Oudar (Eds.), Corrosion Mechanisms in Theory and Practice, Marcel Dekker, Inc., New York, 1995, p. 311.
[4] F.P. Ford, P.L. Andersen, Corrosion in nuclear systems, in: P. Marcus, J. Oudar (Eds.), Corrosion Mechanisms in Theory and Practice, Marcel Dekker, Inc., New York, 1995, p. 547.
[5] L.C. Shao, J.J. Burns, Nucl. Eng. Des. 57 (1980) 133.
[6] W.L. Clarke, G.M. Gordon, Corrosion-NACE 29 (1973) 1.
[7] H. Hännien, I. Aho-Mantila, Effect of sensitization and cold work on stress corrosion susceptibility of austenitic stainless steels in BWR and PWR conditions, Valtion Teknillinen Tutkimuskeskus Technical Research Centre of Finland, Report 88, 1981, p. 1.
[8] J.-A. Le Duff, P. Ould, J.-L. Bernard, Int. J. Pres. Ves. Pip. 65 (1996) 241.
[9] O.S. Tatone, R.L. Tapping, Nucl. Saf. 30 (1989) 382.
[10] J.A. Board, J. Inst. Met. 101 (1973) 241.
[11] K. Varga, Z. Németh, A. Szabó, K. Radó, D. Oravetz, J. Schunk, P. Tilky, F. Körösi, J. Nucl. Mater., in press, doi:10.1016/j.jnucmat.2005.09.012.
[12] L. Kövér, D. Varga, I. Cserny, J. Tóth, K. Tokési, Surf. Interface Anal. 19 (1992) 9.
[13] J. Végh, in: H.J. Mathieu, B. Reihl, D. Briggs (Eds.), Proc. of the 6th European Conference on Applications of Surface and Interface Analysis (ECASIA95), J. Wiley, 1996, p. 679.
[14] K. Varga, The role of interfacial phenomena in the contamination and decontamination of nuclear reactors, Radiotracer Studies of Interfaces, in: G. Horányi (Ed.), Interface Science and Technology, vol. 3, Elsevier B.V., Amsterdam, 2004.
[15] A. Szabó, K. Varga, Z. Németh, K. Radó, D. Oravetz, Mrs. K. É. Makó, Z. Homonnay, E. Kuzmann, P. Tilky, J. Schunk, G. Patek, Corros. Sci., in press.
[16] K. Radó, Z. Németh, K. Varga, J. Schunk, F. Korösi, J. Radioanal. Nucl. Chem., in press.